International Journal of Solids and Structures 274 (2023) 112270

Contents lists available at ScienceDirect

International Journal of Solids and Structures

journal homepage: www.elsevier.com/locate/ijsolstr

Stiff bioinspired architectured beams bend Saint-Venant's principle and generate large shape morphing

Kenichiro Yokota, Francois Barthelat *

Department of Mechanical Engineering, University of Colorado, 427 UCB, 1111, Engineering Dr, Boulder, CO 80309, USA

ARTICLE INFO

Keywords:
Morphing analysis
Saint-Venant's Principle
Discrete element modeling
Bioinspired materials
Fish fin rays

ABSTRACT

Large shape change from localized mechanical actuation is an attractive prospect for morphing materials and structures, but it is limited by Saint-Venant's principle: In typical solids the effects of self-equilibrated loads applied over a small region of the solid rapidly decay away from that region, resulting in highly localized deformations and no shape change. Materials and structures with unusual and/or heterogenous combinations of properties can however overcome this limitation. Fish fins, for example, can undergo large changes in curvature distributed over long distances by simple push–pull forces applied at their base. While this type of morphing actuation is attractive, pathways to similar engineering structures are still not well established. Here we present a relatively simple lattice-based mechanical model for fish fin-like morphing. We show that the first moment of curvature is an accurate and robust measure for morphing. Morphing from push-pull forces requires unusual combinations of axial, shear and bending stiffness which cannot be achieved in traditional lattice structures. We then propose "*meta*-elements" composed of struts in parallel to achieve these combinations of elastic properties. We finally 3D print and test several of these designs to validate the models and to verify these new design guidelines for morphing structures.

1. Introduction

Shape morphing refers to radical changes in component geometry (Ajaj et al., 2016) which involve large amplitudes and/or unusual deformation modes such as auxetics (Bertoldi et al., 2017), or coupling of deformation modes such as compression-induced twist (Frenzel et al., 2017). When large changes of geometry are needed, morphing materials offer more advantages than traditional discrete mechanisms: lower weight, smoother transitions in deformations, better distributed stresses, simpler kinematics, smaller numbers of actuators, higher reliability. A wide range of design strategies, materials and actuation technologies are currently available for engineering morphing materials: metamaterials (Restrepo et al., 2015; Coulais et al., 2016; Sun et al., 2016), origami (Hawkes et al., 2010); kirigami (Cho et al., 2014; Celli et al., 2018), hydrogels (Jeon et al., 2017); hygromorphs (Reyssat and Mahadevan, 2009), pneumatic shape-morphing elastomers (Siéfert et al., 2019). Radical shape change is achieved in these materials, but only by using relatively soft materials and structures that cannot sustain large external forces without excess deformation, collapse or failure. In contrast, stiff and strong structures can be morphed using piezoelectric actuators (Benjeddou, 2007) or shape memory alloys (Rediniotis et al., 2002), but large actuation forces are required and only relatively small morphing amplitudes can be achieved. This conflict between "morphing amplitude" and stiffness from external loads has been a major obstacle to the systematic use of morphing materials in aerospace and other domains (Thill et al., 2008) (Fig. 1a). Shape morphing is also limited by Saint-Venant's principle. For example, consider a homogenous beam made of an isotropic linear elastic material and free of tractions, except at one end which is subjected to a set of self-equilibrated loads. There are stresses and deformations resulting from these loads, but they are highly localized. More specifically they vanish exponentially away from where the loads are applied and over a characteristic decay length $\lambda \sim h$ where h is the height of the beam (Choi and Horgan, 1978; Goodier, 1937). For beams made of sandwich materials (stiff face sheets, more compliant core structure) the characteristic decay length can be larger ($\lambda \sim 3\,h$ (Choi and Horgan, 1978) because the lower stiffness of the core generates a competition of deformation mode with the flexural deformation of the face sheets. In strongly anisotropic materials or fiber reinforced composite this effect can even be greater with a characteristic decay length and up to $\lambda \sim 6\,h$ (Horgan and Simmonds, 1994).

* Corresponding author.
E-mail address: francois.barthelat@colorado.edu (F. Barthelat).

https://doi.org/10.1016/j.ijsolstr.2023.112270
Received 2 August 2022; Received in revised form 24 March 2023; Accepted 18 April 2023
Available online 21 April 2023

These end effects are in general seen as a hindrance which complicates stress analysis in typical applications. However, these effects can also be amplified and exploited to maximize λ in beams, which in effect would generate large shape change from localized actuation. Fish fins are good examples of morphing structure exploiting this effect: The fins do not contain muscles but display large morphing amplitudes, combined with high stiffness from external loads (hydrodynamic forces), fast response times and actuation from the base only (Alben et al., 2007). Fish fins "probably represents the most elaborate and refined adaption to efficient interaction with water that has ever evolved" (Videler, 1993) and as such, they can serve as models for the design of new morphing materials. Individual fish fins are composed of a collagenous membrane stiffened by 10–30 beam-like structures called rays. Each ray has a diameter in the order of ∼ 100 μm with a tapered profile and aspect ratio > 100 (Fig. 1b). The rays are composed of two layers made of bony segments called hemitrichia, which are connected by collagen fibrils embedded in ground gel-like substance (Fig. 1b). A remarkable feature of fish fins is that their curvature can be adjusted solely by muscular actuation from the base of the rays (Fig. 1b). The shear deformation imposed at the base induces competitions between the flexural deformation of the hemitrichia and the shear deformation of the core, over a "morphing length" which approaches the length of the entire fin. Recent studies (Alben et al., 2007; Videler and Geerlink, 1986; Videler, 1977; Hannard et al., 2021; Aiello et al., 2018) have shown that this

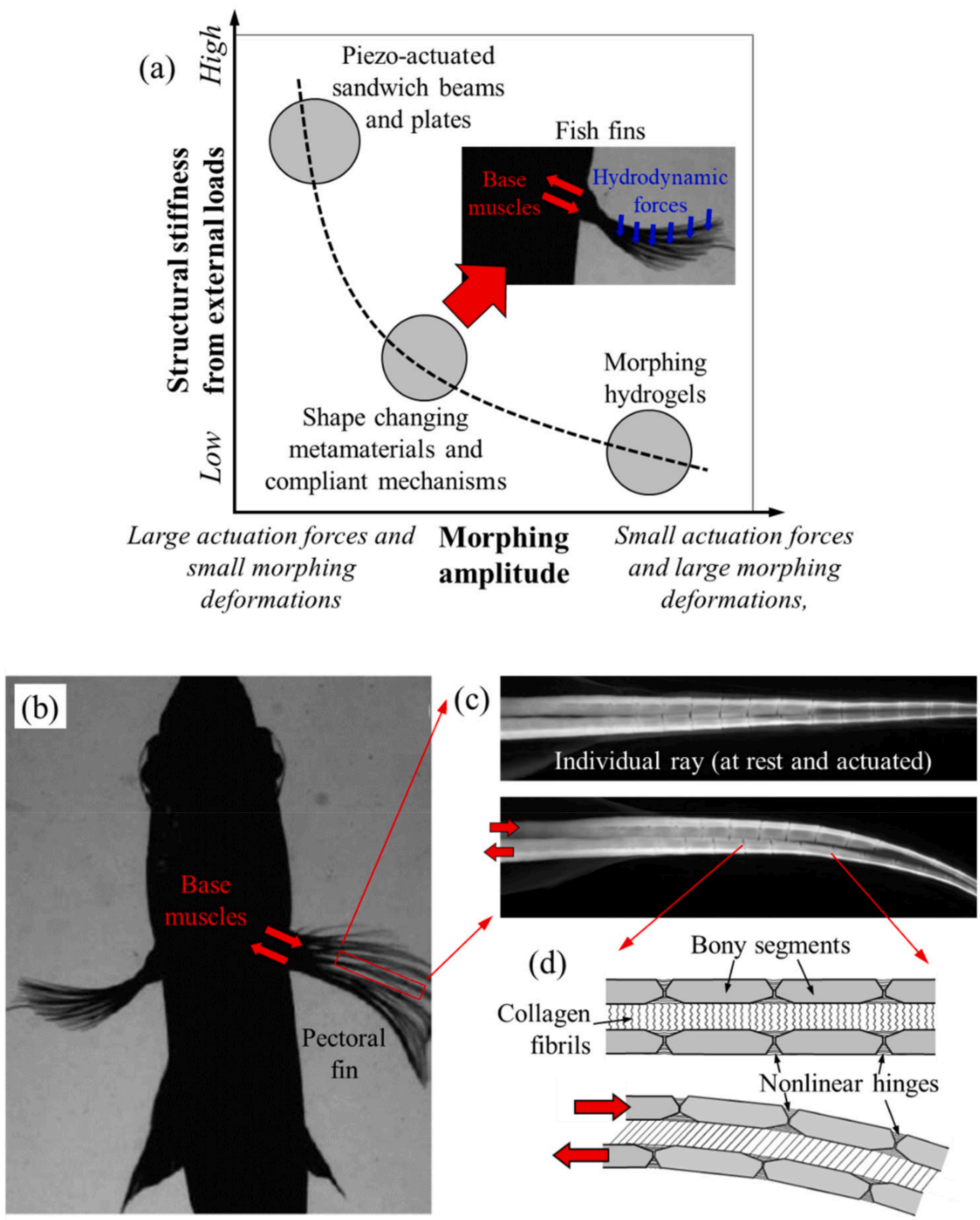

Fig. 1. (a) Morphing amplitude and stiffness from external loads are mutually exclusive in engineering morphing materials, which is hinders their wider use in engineering systems. (b) Fish fins, in contrast, can morph with large amplitude and sustain large external forces. (c) MicroCT scans show the rest position and the actuated position for a caudal fin ray from Atlantic salmon (Salmo salar) (adapted from (Alben et al., 2007; Videler and Geerlink, 1986; Videler, 1977; Hannard et al., 2021); (d) schematic showing the deformation and morphing mechanisms in natural fin rays.

mechanical response can only be achieved with a fine balance between the flexural stiffness of the hemitrichia and the shear stiffness of the core. In addition, individual rays must be stiff to minimize deformations and prevent collapse when subjected to hydrodynamic loads, and the thin hemitrichia must not buckle from the compressive part of the actuation forces. The translation of these structures and morphing mechanisms to synthetic systems has so far been limited (Hannard et al., 2021), and there is a lack of design guidelines and clear pathways to fabrication. Here we present a relatively simple lattice-based mechanical model for fish fin-like morphing, which highlight the fine balance of properties that is required between different parts of the structure. As opposed to previous work on compliant mechanisms (Sun et al., 2013; Verotti et al., 2017) which consider only a point for input and a point for output, we sought to achieve a distributed deformation over the entire beam, which has functional advantage in terms of hydrodynamics, aerodynamics or other robotic applications. We use this model to develop metrics for morphing and design guidelines to achieve morphing with in a beam-like lattice based on "*meta*-elements" with unusual elastic properties. We finally 3D print and test several of these designs to validate the models and to verify the design guidelines.

2. Lattice based ray-like morphing beams based on *meta*-elements

Natural fish rays achieve high morphing amplitude thanks to a fine balance of mechanical properties and distribution of materials, but some of these properties and structures are difficult to duplicate with synthetic materials and fabrication methods. For example, the bony hemitrichia are segmented and joined with complex collagenous hinges (Fig. 1b) which enable unique combinations of flexural stiffness and axial stiffness (Hannard et al., 2021). The core region is composed of crimped collagen fibrils which connect the two hemitrichia, and the extension of these fibrils enables shear strains in excess of 300% in the core region, a mechanical response which is difficult to replicate. As an alternative to these complex materials we sought an easier design and fabrication approach based on discretized elements and lattice structures, which provides several advantages: (i) the discretized approach suits itself to numerical models that can be used to explore large deformations and large rotations; (ii) discrete models can serve as a pathway to a physical realization of the ray based on lattice architecture and (iii) discrete models are suitable for further extensions that can include graded mechanical properties, morphing plates or morphing volumes. Fig. 2 shows the discretized model of a morphing beam that we considered here. In order to simplify the modeling, the design and the fabrication of these structures, we enforced that all elements have the same length (length h) and the same mechanical properties. Numerically the bar elements were treated like Timoshenko beams with an axial stiffness AE, flexural stiffness EI and shear stiffness AG. These can be regarded as local stiffnesses for the beams, which in turn can be used to form the axial element stiffness $\frac{AE}{h}$, the shear element stiffness $1/\left(\frac{h^3}{12EI}+\frac{12h}{AG}\right)$ and the rotational element stiffness $\frac{1+\frac{3EI}{AGh^2}}{\left(\frac{h}{4EI}+\frac{3}{AGh}\right)}$ (Przemieniecki, 2012),where h is the length of the element. Importantly, the effective axial, shear and flexural stiffness of our elements are decoupled from one another in our model. This later feature is crucial to our approach: to achieve high morphing deformation, these "*meta*-elements" will be assigned unusual combinations of axial, flexural and shear stiffness that are not accessible in traditional truss or beam elements. The ray was discretized into square unit cells of dimension $h \times h$ and composed of horizontal and vertical bars elements. The unit cells were repeated N times along the $\times$ direction to create a model of the ray with dimensions $L \times h$ ($L = Nh$). Finally, the two nodes at the base of the ray were subjected to push/pull displacement $\pm u_0/2$, and to zero imposed rotation. With this model in hand, we explored the effects of different combinations of axial, flexural and shear stiffnesses on morphing deformations. Since the elastic deformations in this model are scale-free, we normalized all length by h, and we use the normalized properties $\frac{EI}{AEh^2}$ and $\frac{AG}{AE}$ for the *meta*-elements. The local nodal displacement is $u(s)$ and the local rational angle is $\theta(s)$.

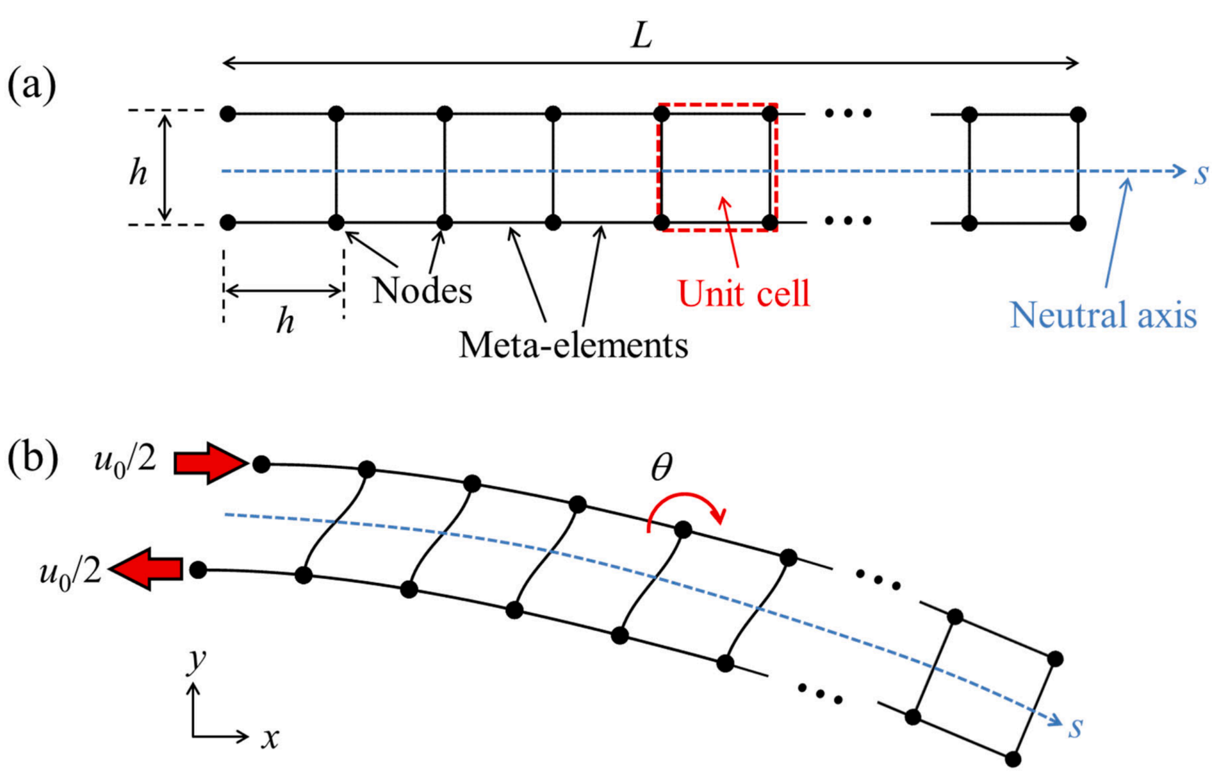

Fig. 2. A discretized, lattice model for fish fin ray-like beams: (a) mesh with dimensions; (b) deformed model when subjected to push/pull displacements at the base nodes.

3. Morphing metrics for fish ray-like beams

An ideal morphing configuration generates curved deformations over long distances over the length of the beam. Hannard et al. (Hannard et al., 2021) defined a "morphing efficiency" obtained by dividing the end deflection of a beam by the actuation force that must be applied at the base to achieve that deflection. This metric was based on end deflection in a way similar to the metric used for compliant mechanisms (Sun et al., 2013; Verotti et al., 2017), and it does not necessarily capture curvature distributed over long distances. Since the curvature along the beam decays exponentially, it is possible to define a decay length for the curvature, which we associated with a "morphing length" L_m. The morphing length was calculated as the distance between the origin and horizontal intercept of a tangent to the deformation plot (Fig. 3). In our lattice based design, the local curvature $\kappa(x, y)$ was numerically calculated using the following procedure: The nodal rotational angle of the four nodes within each cell was first fitted with a bilinear function $\theta(x, y)$, and then the curvature of each cell was simply computed using $\kappa(s) = \frac{\partial\theta}{\partial x}$.

Fig. 4a shows three typical morphing responses we observed by adjusting the properties of the *meta*-elements. Case 1 shows what we define as a "hinge-like" response: The flexural deformations are concentrated near the base of the beam, in a localized "hinge". The rest of the beam remains undeformed, and simply undergoes rigid body translations and rotations. Case 2 shows what we define as "proper morphing", because most of the beam bends from the base displacement. Finally, we also observed Case 3, where the upper and lower elements glide on one another in a "shearing" mode, with no flexural deformation. To systematically assess these various possible morphing responses, we ran 2500 numerical models with $L = 5\ h$, $u_0 = 0.4\ h$ and with a broad range of combination of possible element properties ($\frac{EI}{AEh^2}$ and $\frac{AG}{AE}$). For each model we measured the normalized morphing $\frac{L_m}{h}$, and we display the results on Fig. 4b. This map shows that maximum values for $\frac{L_m}{h}$ occur at the lower right region, that is for $\frac{AG}{AE} < \frac{EI}{AEh^2}$. Indeed, this combination leads to a long morphing distance, but also to very small flexural deformations as the entire structure of the beam mostly produces shear deformation (Case 3 belongs to this region). The morphing length $\frac{L_m}{h}$ is therefore not an adequate measure for morphing deformations.

Another possible metric we considered for morphing is the average (normalized) curvature along the entire beam $h\overline{\kappa}$, computed as:

$$h\overline{\kappa} = \frac{h}{L}\int_0^L \kappa(s)ds = \frac{h}{L}\int_0^L \frac{d\theta(x, y)}{dx}ds \tag{1}$$

Fig. 4c shows a map of the average curvature for all combinations of *meta*-element properties. The average curvature is high for high $\frac{AG}{AE}$ and

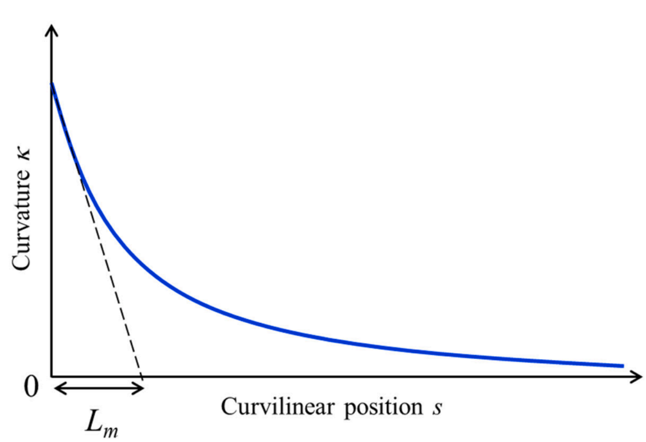

Fig. 3. Local curvature k of a morphed beam as function of curvilinear position s. A "morphing length" L_m can be measured from this plot.

low $\frac{EI}{AEh^2}$, but the corresponding models all lead to a "hinge-like" response (Case 1 on Fig. 4a). The maps of Fig. 4 also show the domain which can be achieved with regular beam elements with "traditional" combinations of AE, AG and EI (how we derived the boundary of this domain is explain below). It is clear that beams made of these traditional elements, corresponding to classical lattice materials, all deform by "hinging" in accordance with Saint-Venant's principle. In these cases the hinge-like response produces high curvatures which occur only over short distances, but which are sufficient to produce high values for the average curvature $h\overline{\kappa}$. $h\overline{\kappa}$ is therefore not an adequate metric for morphing. An adequate metric for morphing should capture curvatures distributed over long distances over the beam. The third metric we considered is therefore the first moment of curvature $\overline{\kappa}^{(1)}$, computed as:

$$\overline{\kappa}^{(1)} = \frac{1}{L}\int_0^L s\kappa ds = \frac{1}{L}\int_0^L s\frac{d\theta(x, y)}{dx}ds \tag{2}$$

With this metric, designs producing curvatures distributed over long distances away from the base of the beam should produce high values of $\overline{\kappa}^{(1)}$. Fig. 4d shows a map of $\overline{\kappa}^{(1)}$, showing that high values of this metric occur along a narrow band of $\frac{AG}{AE}$ and $\frac{EI}{AEh^2}$ combinations. Models taken within this region correspond to case 2 of Fig. 4a, with high morphing curvatures distributed over long distances. We also note that this optimal region ends at the upper right: Indeed if the axial stiffness AE is too low (high $\frac{EI}{AEh^2}$ and $\frac{AG}{AE}$ at the upper right corner of Fig. 4d), the actuation displacement is absorbed by axial deformation of the elements and morphing is suppressed. The maps of Fig. 4 were generated for $L = 5\ h$. Changing the aspect ratio of the beams shifts the location of the best designs on the map, but the general trends shown on Fig. 4 are preserved. For example longer beams ($L = 80\ h$) led to a similar map, but with the region of the highest morphing amplitude shifted towards lower values of $\frac{AGh^2}{EI} = 2\times 10^{-3}$. The 1st moment of curvature $\overline{\kappa}^{(1)}$ is therefore the most appropriate method to evaluate morphing amplitude. We also ran nonlinear versions of the model where large deformations and large rotations were considered using co-rotational elements (Bathe and Bolourchi, 1979; Cav et al., 2009). Fig. 5 shows that the nonlinear models deviate from the linear model by at most 2.3% up to $u_0/h = 0.5$, which shows that the linear model is acceptable within that range of deformation. For larger deformations ($u_0/h = 1$), the error increases to 13% at large actuation. Since linear and nonlinear solutions are relatively close, the maps produced by these two types of models were almost identical.

Considering again the map of Fig. 4d, it is now possible to identify the elastic properties required for high morphing amplitude. The region of highest first moment of curvature for $L = 5\ h$ can be captured by the guidelines:

$$\begin{cases} \dfrac{AGh^2}{EI} = 1 \\ \dfrac{EI}{AEh^2} < 10^{-1} \end{cases} \tag{3}$$

These combinations of properties are unusual and we show next that they cannot be achieved by standard beam elements. Consider the design of Fig. 6a, which is composed of rigid squares at the nodes, connected by regular beam elements of thickness t and width w.

Neglecting local shear deformations in the struts, the equivalent mechanical properties for individual regular beam are given by:

$$\begin{cases} (AE)_{eq}^{beam} = A_{beam}E = Ewt \\ (AG)_{eq}^{beam} = \dfrac{12EI_{beam}}{l^2} = E\dfrac{wt^3}{l^2} \\ (EI)_{eq}^{beam} = EI_{beam} = E\dfrac{wt^3}{12} \end{cases} \tag{4}$$

Note that the equivalent shear stiffness $(AG)_{eq}^{beam}$ for the strut results

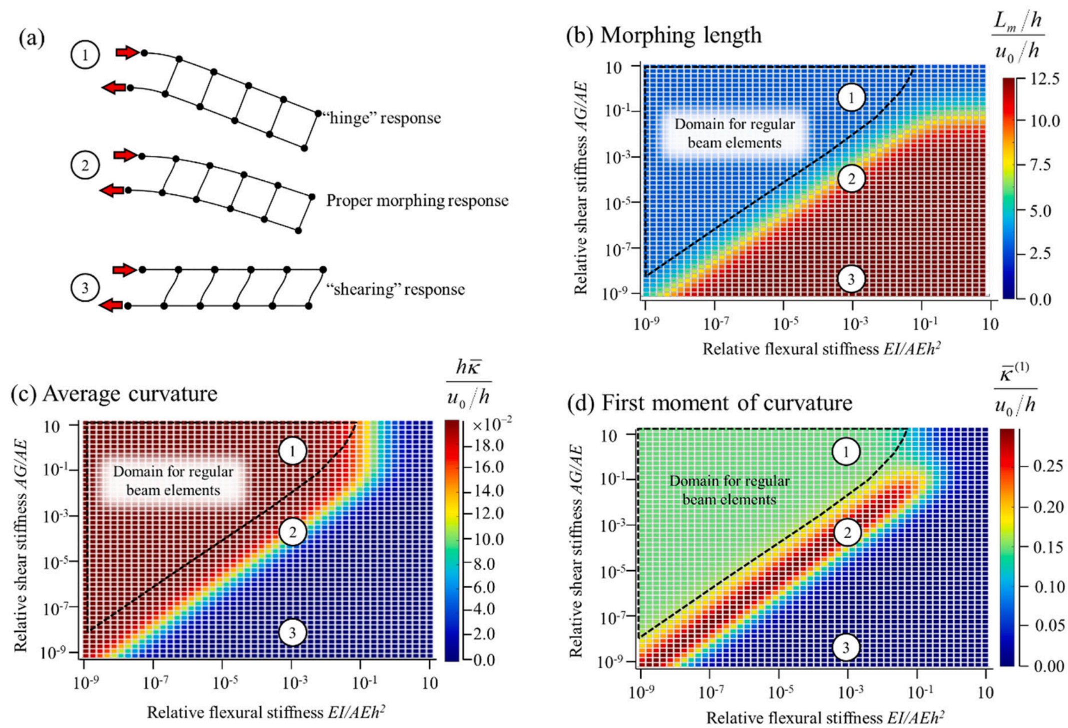

Fig. 4. (a) Typical responses for beams with $L = 5\,h$ made of "*meta*-elements" that use three different combinations of properties; Maps obtained for a broad range of *meta*-element properties and for $L = 5\,h$: (b) morphing length, (c) average curvature and (d) first moment of curvature. The locations for cases 1,2 and 3 are shown on each of the maps.

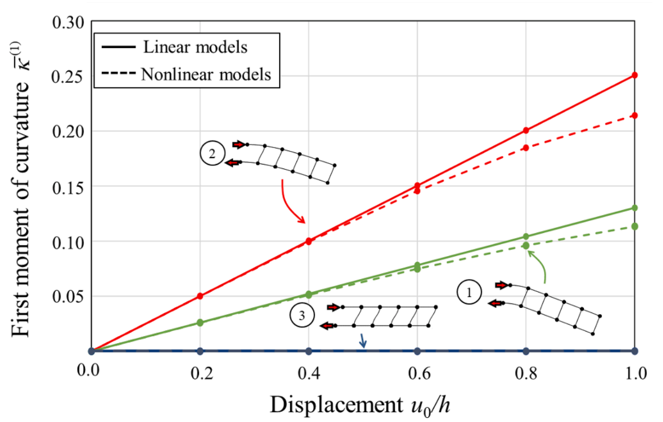

Fig. 5. Comparison of first moments of curvature obtained with linear and nonlinear models on three different designs.

from flexural deformations as illustrated in Fig. 6b, so that it is governed by the shear modulus of the beam but also by EI_{beam}. We then form ratio of elastic properties:

$$\begin{cases} \dfrac{(AG)_{eq}^{beam}}{(AE)_{eq}^{beam}} = \left(\dfrac{t}{l}\right)^2 \\ \dfrac{(EI)_{eq}^{beam}}{(AE)_{eq}^{beam}} = \dfrac{1}{12}\left(\dfrac{t}{h}\right)^2 \end{cases} \tag{5}$$

There are geometrical constraints on t, h and l. The length of the beams cannot exceed h, and the thickness of the strut is limited by the size of the rigid square domains:

$$\begin{cases} 0 < \dfrac{l}{h} < 1 \\ 0 < \dfrac{t}{h} < \dfrac{h-l}{h} \end{cases} \tag{6}$$

The domain corresponding to equations (5) subjected to constraints (6) is shown in on Fig. 4d. This domain cannot reach the optimum morphing region, and models with properties taken in this region all lead to fast decay of deformation typical of Saint-Venant's principle and to hinge-like responses (Case 1 in Fig. 4). Regular structural beam therefore cannot achieve high morphing amplitude, and specific material anisotropies, microstructures or material architectures are therefore required. In natural fish fin rays, high $\frac{EI}{AEh^2}$ ratios can be achieved by segmentation of the bony segments in the hemitrichia (Hannard et al., 2021). In the core regions, collagen fibrils align in the transverse direction (Hannard et al., 2021) probably also give rise to specific anisotropic properties, although this aspect remains to be explored in more depth. In the next section, we use an alternative approach where we propose architectured "*meta*-elements" that can be designed and fabricated to create the desired combinations of element properties.

4. Physical embodiments of "Meta-elements"

Fig. 4 made it clear that morphing beam-like lattice structures made of regular elements cannot achieve proper morphing and all produce "hinge-like" responses. Unusual combinations of properties in *meta*-elements must be used to achieve proper morphing. In this section we develop a possible physical embodiment for these *meta*-elements. The design was guided by the observation that in regular beam elements, the ratio $\frac{AGh^2}{EI}$ is too high for proper morphing. A simple approach to decrease this ratio is then to use several struts in parallel to form each "*meta*-element" (Fig. 7). Indeed, the shear response for N_{strut} identical struts in parallel is proportional to N_{strut}, but the average flexural response can increase faster with N_{strut}. The geometry and arrangement of the struts

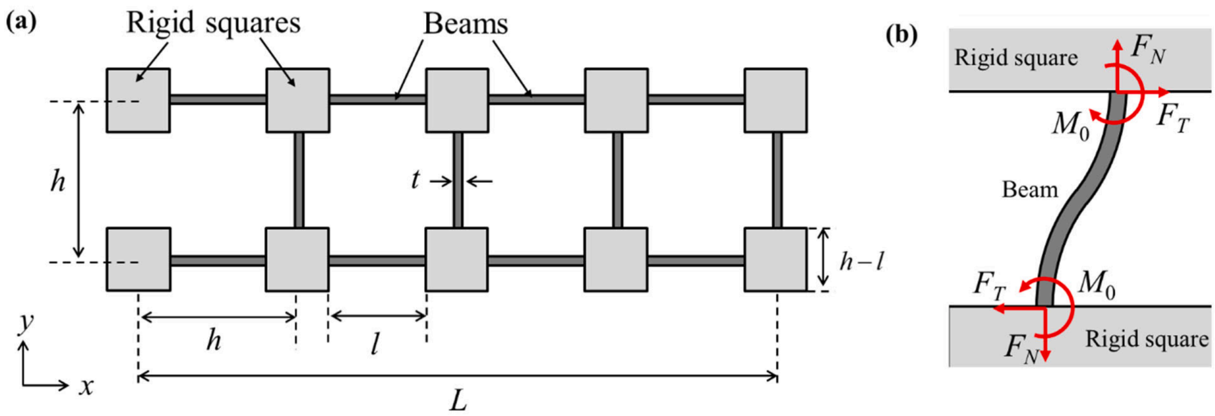

Fig. 6. (a) A morphing beam made of rigid squares and regular beam elements; (b) Loads and deformation of an individual beam.

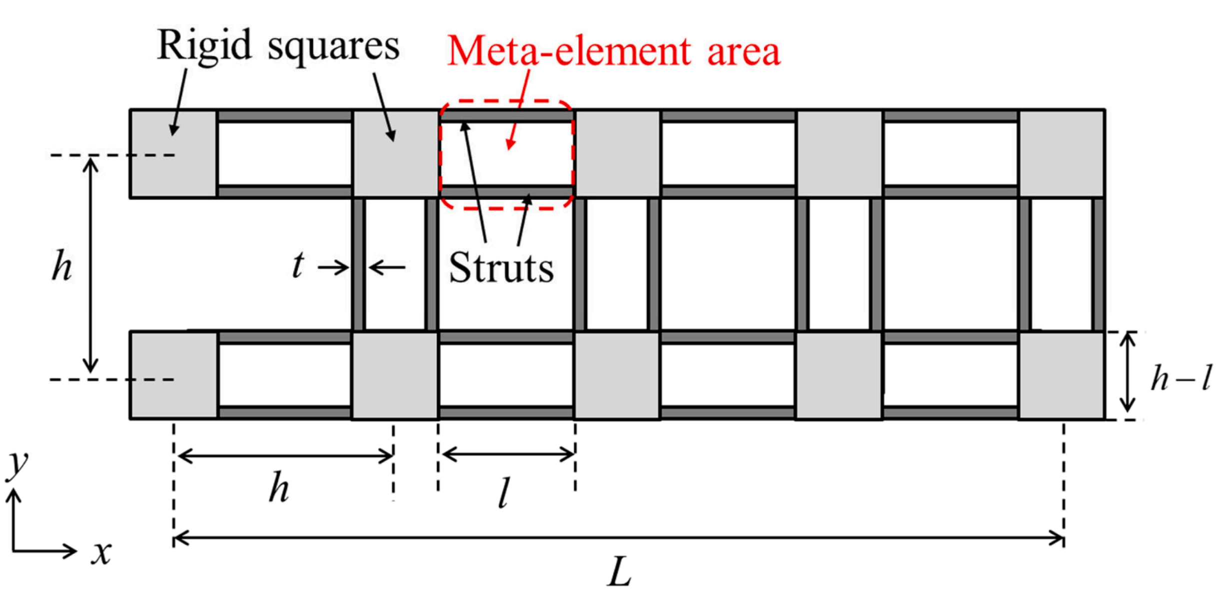

Fig. 7. A beam made of "*meta*-elements" which each consist of two parallel struts.

can therefore be manipulated to obtain the desired properties for the *meta*-elements. In this study we considered the case $N_{strut} = 2$, with the arrangement shown on Fig. 7. Each *meta*-element is made of two parallel struts each with thickness t, depth w and length l.

Neglecting shear deformations in the struts, the axial stiffness $(AE)_{eq}^{strut}$, shear stiffness $(AG)_{eq}^{strut}$ and flexural stiffness $(EI)_{eq}^{strut}$ for the individual struts are identical to equation (4). A *meta*-element made of two parallel struts will have the properties:

$$\begin{cases} (AE)_{eq} = 2Ewt \\ (AG)_{eq} = 2E\dfrac{wt^3}{l^2} \\ (EI)_{eq} = E\dfrac{wt^3}{6} + 2Ewt\left(\dfrac{h-l-t}{2}\right)^2 \end{cases} \tag{7}$$

A key point in equation (7) is that while the axial and shear stiffnesses of two struts are doubled compared to one strut, the flexural stiffness is not only doubled, but also augmented by a term due to axial forces carried by the two struts (following the parallel axis theorem, and in ways similar to I-beams or face-sheet panels). From equation (7) we can then write the ratio of stiffnesses:

$$\begin{cases} \dfrac{(AG)_{eq}}{(AE)_{eq}} = \left(\dfrac{t}{l}\right)^2 \\ \dfrac{(EI)_{eq}}{(AE)_{eq}h^2} = \dfrac{1}{12}\left(\dfrac{t}{l}\right)^2 + \dfrac{1}{4}\left(1 - \dfrac{l}{h} - \dfrac{t}{h}\right)^2 \end{cases} \tag{8}$$

Equation (8) shows how attractive combinations of elastic properties can be achieved for a *meta*-element made of two struts, by manipulating $\frac{l}{h}$ and $\frac{t}{h}$. There are however geometrical constraints on these parameters. The length of the struts cannot exceed the height of the beam, and the thickness of the strut is limited by the size of the rigid square domains:

$$\begin{cases} 0 < \dfrac{l}{h} < 1 \\ 0 < \dfrac{t}{h} < \dfrac{h-l}{2h} \end{cases} \tag{9}$$

The combination of properties made possible in this design and captured by equations (8) under constraints (9) is illustrated in Fig. 8a. This map clearly shows that the optimum combinations of *meta*-element properties can be approached using the two-strut design. Fig. 8b shows four designs taken from that map. In the best designs the spacing between the two struts was maximized to match the size of the rigid square domains, in order to maximize the flexural rigidity of the *meta*-element. For this same reason, the addition of more struts in the *meta*-element did

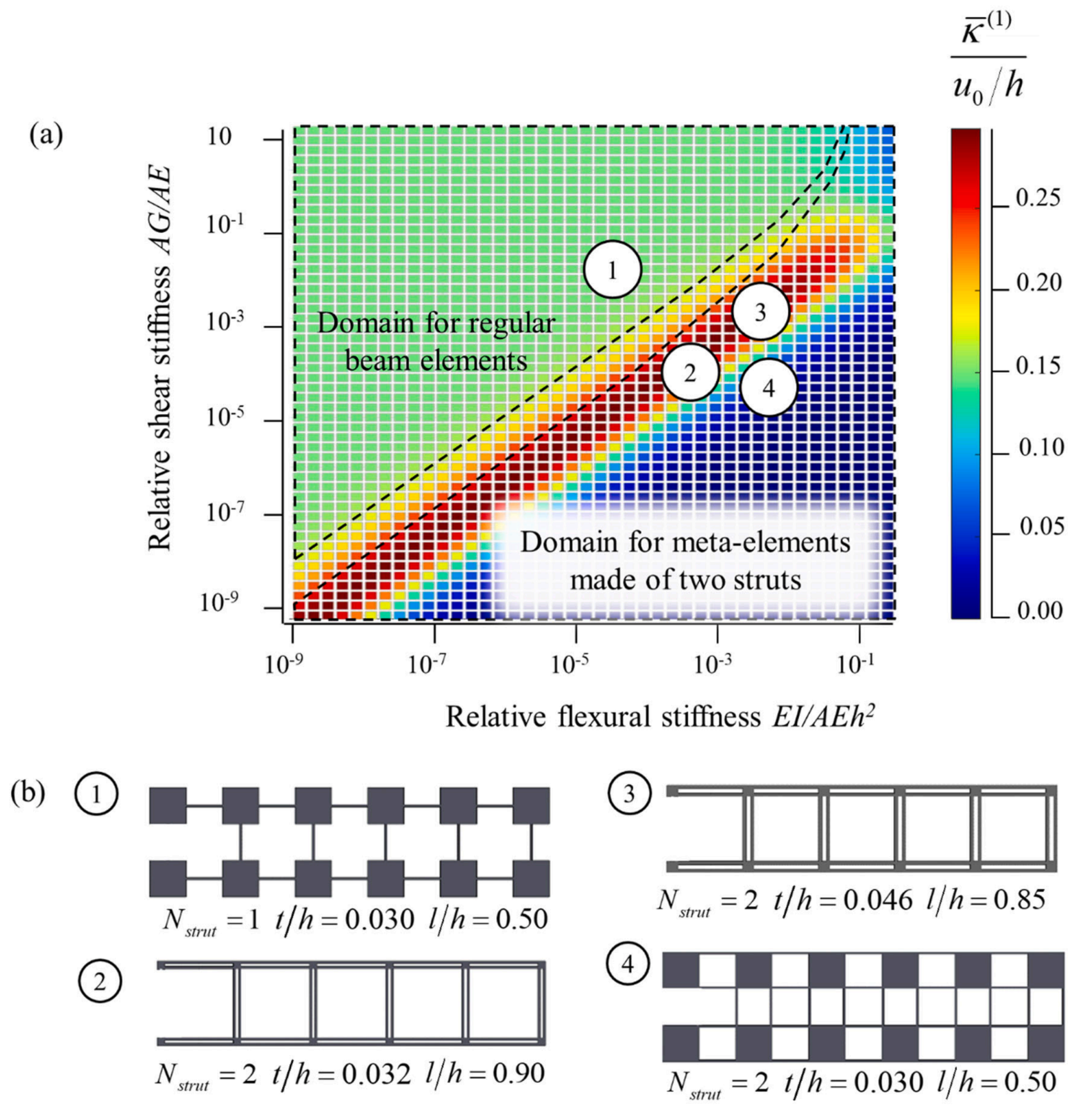

Fig. 8. (a) Map of the first moment of curvature for $L/h = 5$. The domain for regular beam elements and for *meta*-elements made of two struts are shown; (b) Four representative designs taken from that map.

not improve morphing performance. In the next section we fabricate and test the four designs of Fig. 8b.

5. Fabrication and testing of morphing beams

To validate our lattice-based mathematical models and the *meta*-element design approach, we fabricated and tested the four representative designs shown in Fig. 8. The materials were 3D printed using a high-resolution digital light processing (DLP) 3D printer (Envisiontec MicroPlus HD). In addition to high spatial resolution, this printing technology produces fully dense and isotropic components which facilitates mechanical testing and comparisons with models. The 3D-printed material was a photopolymer with a measured elastic modulus of 800 MPa. This material was also enough strong and there was no evidence to show permanent deformations for designs in the highest morphing amplitude and hinge-like design. For the geometry we used $h = 10$ mm and the total lengths of $L = 50$ mm for all designs. Once fabricated, the beams were tested mechanically using a custom micro-testing platform. The lower node at the base was clamped, and the upper node at the base was fixed to a micromanipulator (Sutter Instrument SOLO) controlled by a custom Matlab routine which we used to impose a displacement u_0. The clamps were designed to prevent rotations of the nodes at the base. Finally, the microactuator was mounted with a 50 N load cell used to measure the actuation force F_0. To conduct the morphing experiment the actuation displacement u_0 was increased from zero to a maximum value at a rate of 0.65 mm/s, and then brought back to zero at the same displacement rate.

Fig. 9 shows typical actuation forces F_0 measurements as function of actuation displacement u_0, together with images of the morphing beams acquired during the test. We also show the deformed system as predicted by the finite element model described above (we used the non-linear version of the code to account for the large deflections and rotations observed experimentally). In the experiments we first cycled the actuation displacements using a small amplitude (maximum $u_0 = 2$ mm), which showed a quasi-linear response, with loading and unloading paths that almost coincide. The same beams could be used for multiple morphing tests with repeatable results. We then used larger amplitudes (maximum $u_0 = 10$ mm), and for these cases we observed softening and instabilities due to buckling. In these cases the structures were deformed permanently and could not be re-used. Nevertheless, there were pronounced differences between the four designs. Design 1 is made of regular beam elements, which according to our model should lead to a "hinge" type of response, where the deformation is localized at the base of the structure while the rest just translates and rotate as a rigid body.

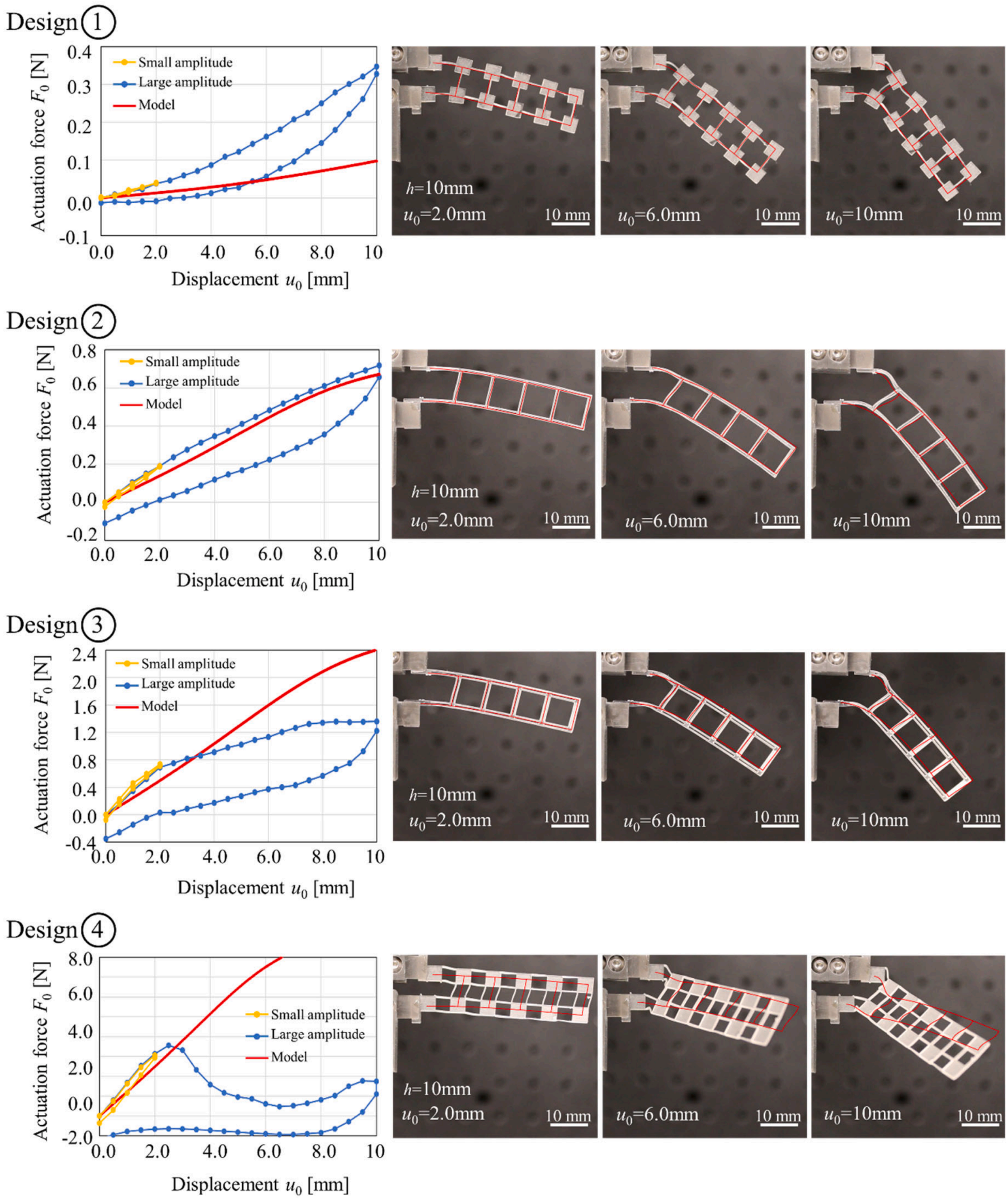

Fig. 9. Results for the four designs shown in Fig. 8. For each design the predicted and measured actuation force–displacement is shown, as well as the predicted and observed deformed structures. Model and experiments agree well, except for cases with large buckling deformations.

Indeed, Fig. 9 shows that Design 1 which hinges at the base, with a deformed shape captured by the model. Design 2 and 3 were chosen in the region which is optimum for morphing (Fig. 8a). Indeed, each of these designs produced a well distributed flexural deformation at small actuation displacements ($u_0 < 2$ mm). However, at larger actuation displacements some of the struts buckled, which limited the morphing capability of the structure (buckling was however well captured in our models). Finally, Design 4 was taken from a suboptimal region (Fig. 8a). The first snapshot for design 4 shows a "shearing" type of response, where the unit cells deform in shear with little or no flexural deformations. At higher actuation displacements severe buckling was observed, which could only be partially captured by the model. Overall, the experiments validate our model based on *meta*-elements, the design based on parallel structures and our optimization approach as long as the actuation displacement remains small. At larger displacement ($u_0 >$ 2 mm) we observed buckling, which limits the efficacy of buckling and damages the structure.

6. Summary

The long decay length in deformation seen in some composites and anisotropic materials is usually perceived as a hindrance. Fish fins show that instead, this effect can be used and amplified to create morphing curvatures over long distances in stiff beams, and only from push-pull action at the base. Morphing in fish fin results from a competition between axial deformations, flexural deformations and shear deformations. In this study we have applied this concept to lattice-based morphing beams that use "*meta*-elements". Lattice-based structures are a convenient platform to systematically explore the effects of element property on morphing. Lattice-based structures can also be used for large deformations and large rotations, and they can easily be extended to morphing plates or even morphing volumes. The main findings in this work are as follows:

(1) The first moment of curvature $\overline{\kappa}^{(1)}$ provides a robust metric for the morphing of beam-like structures which can distinguish between adequate morphing and poor morphing. For example, cases where all deformations concentrate at a hinge near the actuation region produce low values for $\overline{\kappa}^{(1)}$, while cases where morphing curvature are distributed over long distances away from the actuation region produce high values for $\overline{\kappa}^{(1)}$.
(2) The shape morphing of fish ray-like beam over long distances (high $\overline{\kappa}^{(1)}$) requires competitions between different deformation modes over a long distance from the actuation region, in a way that contradict Saint-Venant's principle. To promote this competition the structure must have unusual elastic properties locally, for example high flexural stiffness but low axial stiffness.
(3) Lattice structures with unusual local properties can be modeled using "*meta*-elements" with decoupled and unusual combinations of axial stiffness, flexural stiffness and shear stiffness. These models can be used to identify which combinations of these properties lead to the most effective morphing.
(4) Physical embodiments of these *meta*-elements can be achieved by structural design and architecture. Here we have shown that high flexural stiffness and low axial stiffness can be achieved by using two struts in parallel.
(5) We fabricated and tested lattice beams made of these *meta*-elements. Their morphing response was superior to lattice structures made of regular beam elements.
(6) The experiments show that the limiting factor for the morphing response is buckling of the struts. Buckling can be captured with our finite element model, and in the future it could be considered at the design optimization stage.

For this study we limited ourselves to morphing beams actuated with push/pulls at the base. The method can however be extended to more complex 2D and 3D structures, and to other actuation methods, including multiple actuation regions. This effort may lead to new designs for active morphing materials that can be actuated locally, and which combine high morphing amplitude (i.e. large deformation and low actuation forces) with high stiffness from external forces. Previous work on compliant mechanisms (Sun et al., 2013; Verotti et al., 2017) only consider one point for input and one point for output, used for example to maximize the amplification of displacements. The approach we took here was to instead achieve a distributed deformation over the entire beam as an output, which has functional advantage in potential applications that include shape morphing medical tools (microsurgical tools and catheters), energy (morphing wind turbine blades), aerospace (morphing wings, deployable space vehicles), marine propulsion (morphing propellers), or robotics (stiff morphing for high grasping force).

CRediT authorship contribution statement

Kenichiro Yokota: Conceptualization, Methodology, Software, Validation, Formal analysis, Investigation, Data curation, Writing – original draft, Visualization. **Francois Barthelat:** Conceptualization, Methodology, Software, Writing – review & editing, Supervision, Project administration, Funding acquisition.

Declaration of Competing Interest

The authors declare that they have no known competing financial interests or personal relationships that could have appeared to influence the work reported in this paper.

Data availability

Data generated for this study are available from the corresponding author on reasonable request.

Acknowledgments

This work was supported by the College of Engineering and by the Department of Mechanical Engineering at the University of Colorado at Boulder. K.Y. was supported by the Japan Ministry of Defense. The authors gratefully acknowledge Saurabh Das for his assistance setting up the morphing experiments.

References :

Aiello, B.R., Hardy, A.R., Cherian, C., Olsen, A.M., Orsbon, C.P., Hale, M.E., Westneat, M. W., 2018. A comparison of pectoral fin ray morphology and its impact on fin ray flexural stiffness in labriform swimmers. J. Morphol. 279 (8), 1031–1044.
Ajaj, R.M., Beaverstock, C.S., Friswell, M.I., 2016. Morphing aircraft: The need for a new design philosophy. Aerosp. Sci. Technol. 49, 154–166.
Alben, S., Madden, P.G., Lauder, G.V., 2007. The mechanics of active fin-shape control in ray-finned fishes. J. R. Soc. Interface 4 (13), 243–256.
Bathe, K.-J., Bolourchi, S., 1979. Large displacement analysis of three-dimensional beam structures. Int. J. Numer. Meth. Eng. 14 (7), 961–986.
Benjeddou, A., 2007. Shear-mode piezoceramic advanced materials and structures: a state of the art. Mech. Adv. Mater. Struct. 14 (4), 263–275.
Bertoldi, K., Vitelli, V., Christensen, J., Van Hecke, M., 2017. Flexible mechanical metamaterials. Nature Rev. Mater. 2, 1–11.
Cav, Y., Paik, J.K., Atluri, S.N., 2009. Large deformation analyses of space-frame structures, with members of arbitrary cross-section, using explicit tangent stiffness matrices, based on a von Karman type nonlinear theory in rotated reference frames. Computer Modeling Eng. Sci. (CMES) 53, 123.
Celli, P., McMahan, C., Ramirez, B., Bauhofer, A., Naify, C., Hofmann, D., Audoly, B., Daraio, C., 2018. Shape-morphing architected sheets with non-periodic cut patterns. Soft Matter 14 (48), 9744–9749.
Cho, Y., Shin, J.-H., Costa, A., Kim, T.A., Kunin, V., Li, J.u., Lee, S.Y., Yang, S., Han, H.N., Choi, I.-S., Srolovitz, D.J., 2014. Engineering the shape and structure of materials by fractal cut. Proc. Natl. Acad. Sci. U.S.A. 111 (49), 17390–17395.
Choi, I., Horgan, C.O., 1978. Saint-Venant end effects for plane deformation of sandwich strips. Int. J. Solids Struct. 14 (3), 187–195.
Coulais, C., Teomy, E., de Reus, K., Shokef, Y., van Hecke, M., 2016. Combinatorial design of textured mechanical metamaterials. Nature 535 (7613), 529–532.
Frenzel, T., Kadic, M., Wegener, M., 2017. Three-dimensional mechanical metamaterials with a twist. Science 358 (6366), 1072–1074.
Goodier, J.N., 1937. A general proof of Saint-Venant's principle. The London, Edinburgh, Dublin Phil. Magazine J. Sci. 23 (155), 607–609.
Hannard, F., Mirkhalaf, M., Ameri, A., Barthelat, F., 2021. Segmentations in fins enable large morphing amplitudes combined with high flexural stiffness for fish-inspired robotic materials. Sci. Robotics 6, eabf9710.
Hawkes, E., An, B., Benbernou, N.M., Tanaka, H., Kim, S., Demaine, E.D., Rus, D., Wood, R.J., 2010. Programmable matter by folding. Proc. Natl. Acad. Sci. U.S.A. 107 (28), 12441–12445.
Horgan, C.O., Simmonds, J.G., 1994. Saint-Venant end effects in composite structures. Compos. Eng. 4 (3), 279–286.
Jeon, S.-J., Hauser, A.W., Hayward, R.C., 2017. Shape-morphing materials from stimuli-responsive hydrogel hybrids. Acc. Chem. Res. 50 (2), 161–169.
Przemieniecki, J.S., 2012. Theory of Matrix Structural Analysis, Revised edition. Dover Publications, New York.
Rediniotis, O.K., Wilson, L.N., Lagoudas, D.C., Khan, M.M., 2002. Development of a shape-memory-alloy actuated biomimetic hydrofoil. J. Intell. Mater. Syst. Struct. 13 (1), 35–49.

Restrepo, D., Mankame, N.D., Zavattieri, P.D., 2015. Phase transforming cellular materials. Extreme Mech. Lett. 4, 52–60. https://doi.org/10.1016/j.eml.2015.08.001.
Reyssat, E., Mahadevan, L., 2009. Hygromorphs: from pine cones to biomimetic bilayers. J. R. Soc. Interface 6 (39), 951–957.
Siéfert, E., Reyssat, E., Bico, J., Roman, B., 2019. Bio-inspired pneumatic shape-morphing elastomers. Nat. Mater. 18 (1), 24–28.
Sun, X., Chen, W., Tian, Y., Fatikow, S., Zhou, R., Zhang, J., Mikczinski, M., 2013. A novel flexure-based microgripper with double amplification mechanisms for micro/nano manipulation. Rev. Sci. Instrum. 84 (8), 085002.
Sun, J., Guan, Q., Liu, Y., Leng, J., 2016. Morphing aircraft based on smart materials and structures: A state-of-the-art review. J. Intell. Mater. Syst. Struct. 27 (17), 2289–2312.
Thill, C., Etches, J., Bond, I., Potter, K., Weaver, P., 2008. Morphing skins. The. Aeronaut. J. 112 (1129), 117–139.
Verotti, M., Dochshanov, A., Belfiore, N.P., 2017. A Comprehensive Survey on Microgrippers Design: Mechanical Structure. J. Mech. Des. 139. https://doi.org/10.1115/1.4036351.
Videler, J.J., 1977. Mechanical properties of fish tail joints. Fortschr Zool 24, 183–194.
Videler, J.J., 1993. Fish swimming, vol. 10. Springer Science & Business Media.
Videler, J.J., Geerlink, P.J., 1986. The relation between structure and bending properties of teleost fin rays. Netherlands J. Zool. 37 (1), 59–80.